

Article

# Investigation of Hydrodynamic Forces for Floating Offshore Wind Turbines on Spar Buoys and Tension Leg Platforms with the Mooring Systems in Waves

Yu-Hsien Lin \*, Shin-Hung Kao and Cheng-Hao Yang

Department of Systems and Naval Mechatronic Engineering, National Cheng Kung University, No. 1, University Rd., Tainan City 70101, Taiwan; lsaox50289@gmail.com (S.-H.K.); dadaorange12345@gmail.com (C.-H.Y.)

\* Correspondence: vyhlin@mail.ncku.edu.tw; Tel.: +886-6-2757575 (ext. 63542)

Received: 28 December 2018; Accepted: 4 February 2019; Published: 12 February 2019



**Abstract:** This study aims to develop a modularized simulation system to estimate dynamic responses of floating Offshore Wind Turbines (OWTs) based on the concepts of spar buoy and Tension Leg Platform (TLP) corresponding with two typical mooring lines. The modular system consists of the hydrodynamic simulator based the Cummins time domain equation, the Boundary Element Method (BEM) solver based on the 3D source distribution method, and an open-source visualization software ParaView to analyze the interaction between floating OWTs and waves. In order to realize the effects of mooring loads on the floating OWTs, the stiffness and damping matrices are applied to the quasi-static mooring system. The Response Amplitude Operators (RAOs) are compared between our predicted results and other published data to verify the modularized simulation system and understand the influence of mooring load on the motion responses in regular or irregular waves. It is also demonstrated that the quasi-static mooring system is applicable to different types of mooring lines as well as determining real-time motion responses. Eventually, wave load components at the resonance frequencies of different motion modes for selected floating OWTs would be present in the time domain.

**Keywords:** floating offshore wind turbine; mooring system; RAO; panel method; modular system; offshore wind

## 1. Introduction

Compared with the fixed-type Offshore Wind Turbines (OWTs), the advantages of the floating OWTs are more suitable for mass production and easy to install offshore. They can be roughly divided into three primary concepts, spar buoy, TLP, and barge, in terms of how they achieve the basic stability [1]. The spar buoy maintains the stability of the platform from a deep draft. The original spar buoy, developed by Statoil of Norway [2], is called Hywind, and the bottom is connected by three catenary mooring lines. The stability of Hywind can be enhanced by adding the ballast water. The TLP maintains its stability basically by way of a mooring system and buoyancy [3]. The requirement of ballast for TLP is relatively low compared with the other concepts, but the design of the mooring system is the most complex. Since the vertical direction of the mooring lines corresponding to TLP needs to be subjected to large force, the requirement of the mooring system for stability is the most high. Bachynski and Moan [4] indicated that the performance of TLP can be improved in different environmental conditions and water depths by using several design parameters like ballast, pretension, and pontoon radius. On the other hand, the barge maintains stability by using a large water plane and shallow draft. The concept of the barge is a flat-bottom platform, which has a large waterline area and a high restoring stiffness [5]. Another hybrid concept is semi-submersible [6,7], which is mainly

composed of structural columns connected with the pontoons and the operating deck. The operating deck is located high above the sea level due to the good stability of the design, and thus is kept away from the waves.

Butterfield and Musial [8] suggested that the stability of floating OWTs be increased with help of mooring system, ballast and floating platform. There are three common mooring configurations, including taut-leg, catenary, and semi-taut mooring systems [9]. The taut-leg mooring system is usually used with the TLP, whereas the catenary mooring system is used with the spar buoy, the semi-submersible, and the barge floating platforms. The other concept of the mooring system is the semi-taut mooring system, which is a mix between the characteristics mentioned above, though this configuration is less common. Chen and Tarp-Johansen [10] indicated that the catenary mooring lines hanging horizontally at the seabed are capable of sharing the external forces over their lengths. Al-Solihat and Nahon [11] explained that the taut-leg mooring line does not contact the seabed and is taut due to the pretension caused by the platform excess buoyancy. The restoring forces are generated mostly by line elasticity. For the same size and weight of the platform, the mooring radius of the taut-leg system is smaller than that of the catenary mooring system. Semi-taut moorings are also used on some semi-submersibles, consisting of synthetic fibers, chains, or wire moorings. More specifically, the mooring system consists of three parts: an anchor system, a mooring line and a specific mooring layout. The mooring layout depends on the local environmental conditions and the purpose of the offshore unit. Since it is quite complicated to calculate the mooring load, the mooring system is usually defined as a rigid body fixed on the seabed. In addition, the whole system is assumed to be a homogeneous material, so it can be regarded as the product of the linearized restoring matrix and motion responses of the floating unit. In case of neglecting inertia and damping forces in the mathematical model, the computing speed can be enhanced by considering elastic stiffness and effective stiffness in the stiffness matrix [12].

The quasi-static approach like DeepC [13] used for solving the quasi-static mooring system considers the relationship between displacement and force regardless of heave motion, inertia and damping effect of mooring lines. After neglecting the stiffness of bending moment and torque in the calculation of mooring load, Aamo and Fossen [14] developed a finite element model for a mooring line suspended in water by conjecturing Initial Boundary Value Problem (IBVP). While the boundary-value problems are resolved through the Direct Search method [15], the mooring load on the floater can be obtained accompanied with coupling relationship of 6-DOF motion. In order to calculate hydrodynamic forces of the floater, the three-dimensional potential flow method [16–18], including steady and unsteady terms, was applied. For solving steady-state problems, the translating sources are distributed over the floater by the panel method [19] and the complex plane contour integral algorithm [20]. Moreover, the pulsating sources are suggested by adopting the panel method and the series expansion method [21]. Translating sources are used to obtain the wave profiles in the steady-state, whereas pulsating sources are adopted to resolve 6-DOF wave exciting forces in the diffraction problem. Accordingly, the hydrodynamic coefficients, including added masses and damping coefficients, are calculated by simplifying dynamic boundary conditions in the radiation problem [22]. On the other hand, the wave-body-seabed interaction problems have been formulated and solved in variable bathymetry regions with different water depths by a suitable extension of the BEM to 3D [2]. In a recent study [3], it was also demonstrated that the variations of bottom boundaries have significant influences on hydrodynamic coefficients and responses of the floating body with all degrees of freedom.

Since it is challenging to simulate motion responses of marine structures, this study upgraded a modular system [18] to simplify programming and calculation. Modularization can be thought of as the predecessor of object-oriented technology, which shortens the processing time and makes the program more flexible. Another advantage is that the program can be divided into multiple sub-systems, which have compatible interfaces for integration. Modularization also has the characteristics of standardization and severability. Objects that can be combined and disassembled

with the task are compatible with each other for the sake of simplified programs. Hence, the complete program can be considered a collection of modules. At present, the well-known modular system is ETAP Wind Turbine Modeling (WTM) software [23], which is used to design and monitor wind farms in a flexible graphic interface optimized for wind power simulation and analysis. Andersen, Hindhede [24] indicated that the Swim-Motion-Lines (SML) software suite is applicable to the maritime and offshore industries for calculating motion responses of floating platforms in winds, waves, or currents. SML is composed of three modules: the SWIM module is used to calculate hydrodynamic forces in the frequency domain; the MOTION module is adopted to simulate a slow-drift response in the time domain; and the LINES module is employed to estimate the influence of the mooring system on the floating platform. In order to resolve the hydrodynamic coefficients of floaters with complex shapes in waves, the computer program WAMIT (Wave Analysis at MIT), based on the panel method, has been applied [25].

In the following, Section 2 mainly addresses the particulars of four floating platforms and the corresponding mooring systems; Section 3 introduces the running procedure and functions of the modular system; Section 4 presents the background theory of the mathematical model; Section 5 discusses the analyzed results of hydrodynamic coefficients for four floating OWTs; Section 6 exhibits the dynamic responses of floating OWTs compared with other codes or experimental data. Finally, concluding remarks are given in Section 7.

## 2. Platform Configuration and Mooring Layout

In this study, the simulated floating platforms contain a spar buoy at two different water depths, i.e., the OC3-Hywind spar at a depth of 320 m and the UMaine spar at 200 m; and two TLPs, i.e., the MIT/NREL TLP and the UMaine TLP. The aforementioned floating platforms were designed specifically to support the NREL 5-MW wind turbine [26], including the rotor, nacelle, and tower. Meanwhile, properties of mooring systems including taut-leg and catenary lines for the simulated floating platforms [1] are also presented. The particulars of four floating platforms with respect to the mooring properties are given in Table 1.

**Table 1.** Main particulars of floating platforms and mooring systems (SWL: seawater level).

	OC3-Hywind Spar	UMaine-Hywind Spar	MIT/NREL TLP	UMaine TLP
Water Depth (m)	320	200	200	200
Diameter (m)	6.5–9.4	6.5–9.4	18	6.5 (upper column)/ 15 (lower column)
Draft (m)	120	120	47.89	24
Mass, including ballast (kg)	$7.466 \times 10^6$	$7.466 \times 10^6$	$8.6 \times 10^6$	$7.7494 \times 10^5$
CM location of the platform below SWL (m)	89.92	89.92	40.61	19.72
Roll inertia about CM ( $\text{kg} \cdot \text{m}^2$ )	$4.229 \times 10^9$	$4.229 \times 10^9$	$5.716 \times 10^8$	$1.5078 \times 10^8$
Pitch inertia about CM ( $\text{kg} \cdot \text{m}^2$ )	$4.229 \times 10^9$	$4.229 \times 10^9$	$5.716 \times 10^8$	$1.5078 \times 10^8$
Yaw inertia about CM ( $\text{kg} \cdot \text{m}^2$ )	$1.642 \times 10^8$	$1.642 \times 10^8$	$3.614 \times 10^8$	$9.885 \times 10^7$
Mooring System	Catenary	Catenary	Taut-Leg	Taut-Leg
Number of mooring lines	3	3	8 (4 pairs)	3
Un-stretched line length (m)	902.2	468	151.7	171.4
Line diameter (m)	0.09	0.09	0.127	0.222
Line mass density (kg/m)	77.71	145	116	302.89
Line extensional stiffness (N)	$3.842 \times 10^8$	$3.842 \times 10^8$	1,500,000,000	7,720,000,000

### 2.1. OC3-Hywind Spar/UMaine-Hywind Spar

The OC3-Hywind spar is a floating platform that was preliminarily developed in the Offshore Code Comparison Collaboration (OC3). By adopting the concept of the spar buoy “Hywind” from StatoilHydro of Norway, it includes adaptations suitable for supporting the NREL 5-MW machinery and appropriate for public application. In order to distinguish it from the original Hywind concept, it is referred to as the OC3-Hywind spar. The configuration of the OC3-Hywind spar features a deeply drafted, slender spar buoy at a depth of 320 m with three catenary mooring lines. The mooring lines are attached to the floating platform by means of a delta connection to increase the yaw stiffness of the

moorings. The dimensions of the OC3-Hywind spar and the layout of the catenary mooring system are illustrated in Figure 1.

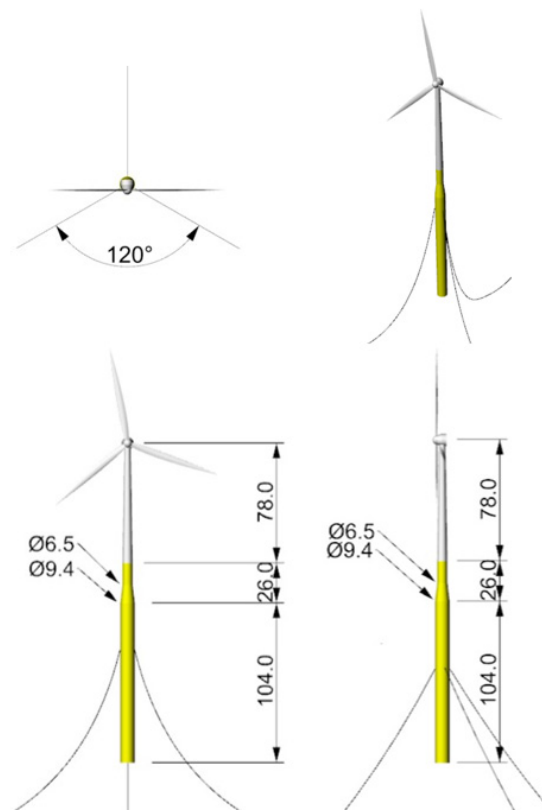


**Figure 1.** The schematic diagrams of the NREL 5MW wind turbine mounted on the OC3-Hywind or UMaine-Hywind spar with the catenary mooring system in different views. (Unit: m).

Similar to the configuration of the OC3-Hywind spar, the UMaine-Hywind spar is drafted at a depth of 200 m rather than 320 m. Therefore, slight modifications of the mooring system and the modes of the tower are required. The difference of water depth between the OC3-Hywind spar and the UMaine-Hywind spar is due to the fact that the University of Maine demonstration project seeks to examine the response of its three generic designs at the same water depth.

The catenary configuration is one of the most common mooring systems with long steel chains whose weight and curved shape hold the floating platform in place. It has long mooring lines partly resting on the seabed to reduce horizontal loads on the anchors. Although the weight of mooring lines limits motion responses of the floating platform, it has greater freedom of movement than the other configurations. The installation procedure of the catenary mooring system is relatively simple. Lower section of catenary mooring lines would result in more disruption of the seabed.

## 2.2. MIT/NREL TLP

The MIT/NREL TLP [12], which is a floating platform derived from modifications to a TLP designed at the Massachusetts Institute of Technology (MIT), is a cylindrical platform ballasted with concrete and moored by four pairs of vertical tendons in tension. Each pair of tendons linked with a spoke radiating horizontally from the bottom of the floating platform. The concrete ballast is adopted to make certain that the MIT/NREL TLP remains stable in mild sea conditions.

Generally, the taut-leg mooring system applied to the MIT/NREL TLP is made of synthetic fibers or wires that use the buoyancy of the floater and firm anchor to the seabed to maintain high tension for stability. It is characterized by vertical loading at anchoring point. Since the taut-leg mooring system is usually perpendicular to the seabed, it is required that anchors withstand large vertical

forces. The horizontal movement of the floating platform is very small due to the fact that high tension limits motion responses to maintain stability. Small horizontal movement also leads to minimal disruption to the seabed. The installation procedure of the catenary mooring system is very challenging. The dimensions of the MIT/NREL TLP and the layout of the taut-leg mooring system are illustrated in Figure 2.

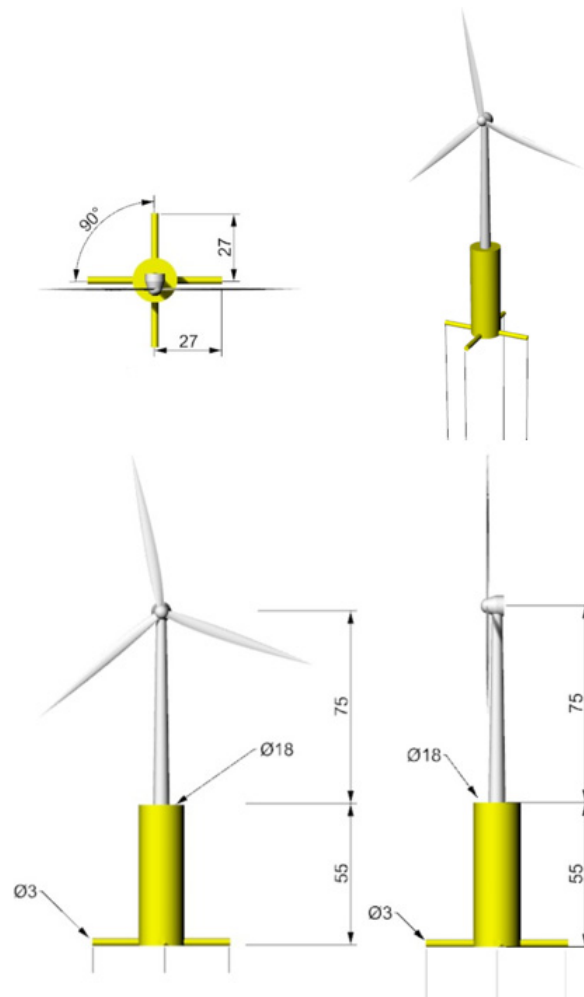


**Figure 2.** The schematic diagrams of the NREL 5MW wind turbine mounted on the MIT/NREL TLP with the taut-leg mooring system in different views. (Unit: m).

### 2.3. UMaine-Hywind TLP

In terms of the weight and the size, the UMaine TLP is much smaller and lighter than the MIT/NREL TLP. It is also a ballasted cylindrical platform, except for only three legs protruding from this base. The vertical tensioned tendon extends from the tip of each leg to the seabed, to which it is anchored. As a result of excess buoyancy, the total tension of the mooring system for the UMaine TLP is less than half of the tension for the MIT/NREL TLP. The tower properties of the NREL 5-MW wind turbine were modified to conform to the UMaine TLP. The dimensions of the UMaine TLP and the layout of the taut-leg mooring system are shown in Figure 3.

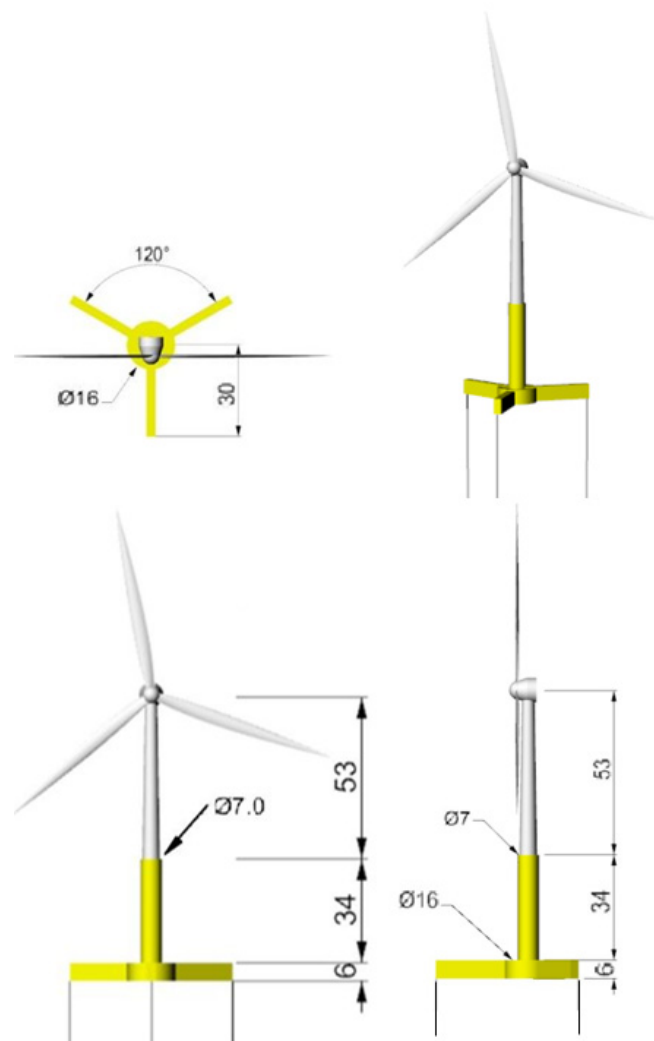


**Figure 3.** The schematic diagrams of the NREL 5MW wind turbine mounted on the UMaine TLP with the taut-leg mooring system in different views. (Unit: m).

### 3. Structure of Modular System

This study intends to develop a modular system for floating OWTs based on MATLAB/SIMULINK in combination with BEM solver and visualization software ParaView as shown in Figure 4. The function of BEM solver is to obtain hydrodynamic coefficients for subsequent 6-DOF motion responses. It can be solved by the boundary element method and by defining the linear free surface. Since BEM solver is established based on the potential flow theory, the influence of viscous force could be ignored. ParaView is an open-source program that combines different codes for visualization of data analysis, and enhances visualization of the flow field as well as 3D modeling.

The present modular system is composed of four modules, including floater module, coordinate module, motion module and mooring module as indicated in Figure 5. The functions of floater module include calculation capabilities of hydrostatic and hydrodynamic forces. While the particulars like mass, Center of Gravity (COG), inertia moment, hydrodynamic coefficients and dimensions of a floating body are given, wave exciting force, radiation added-mass force, radiation damping force, and restoring force would be calculated. Coordinate module can be used to define earth coordinate system, body-fixed coordinate system, gravity, seawater density, wave spectrum, and simulation time length. Motion module is configured to construct displacements, velocities, and accelerations of single or coupling 6-DOF motion responses. The characteristics of the mooring module are designed to select

the stiffness matrix of the mooring system according to the user’s requirement. The mooring load in the time domain can be determined by means of a  $6 \times 6$  linear stiffness matrix and pretension force.

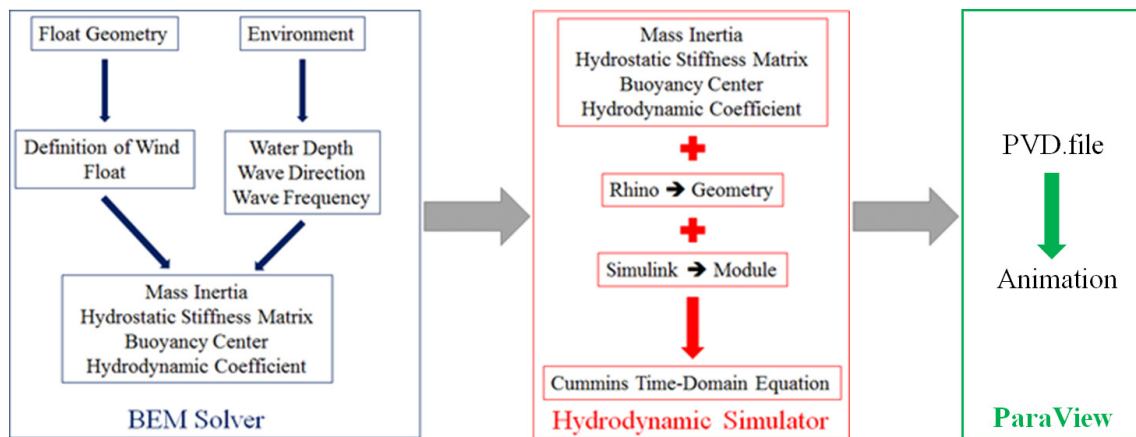


Figure 4. A flowchart of the modular system.

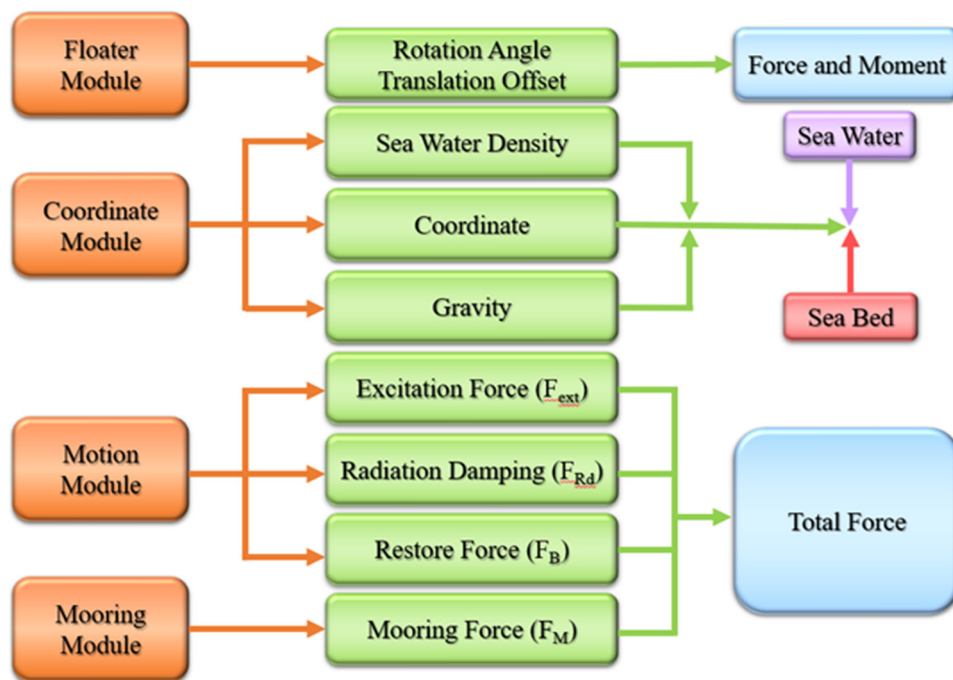
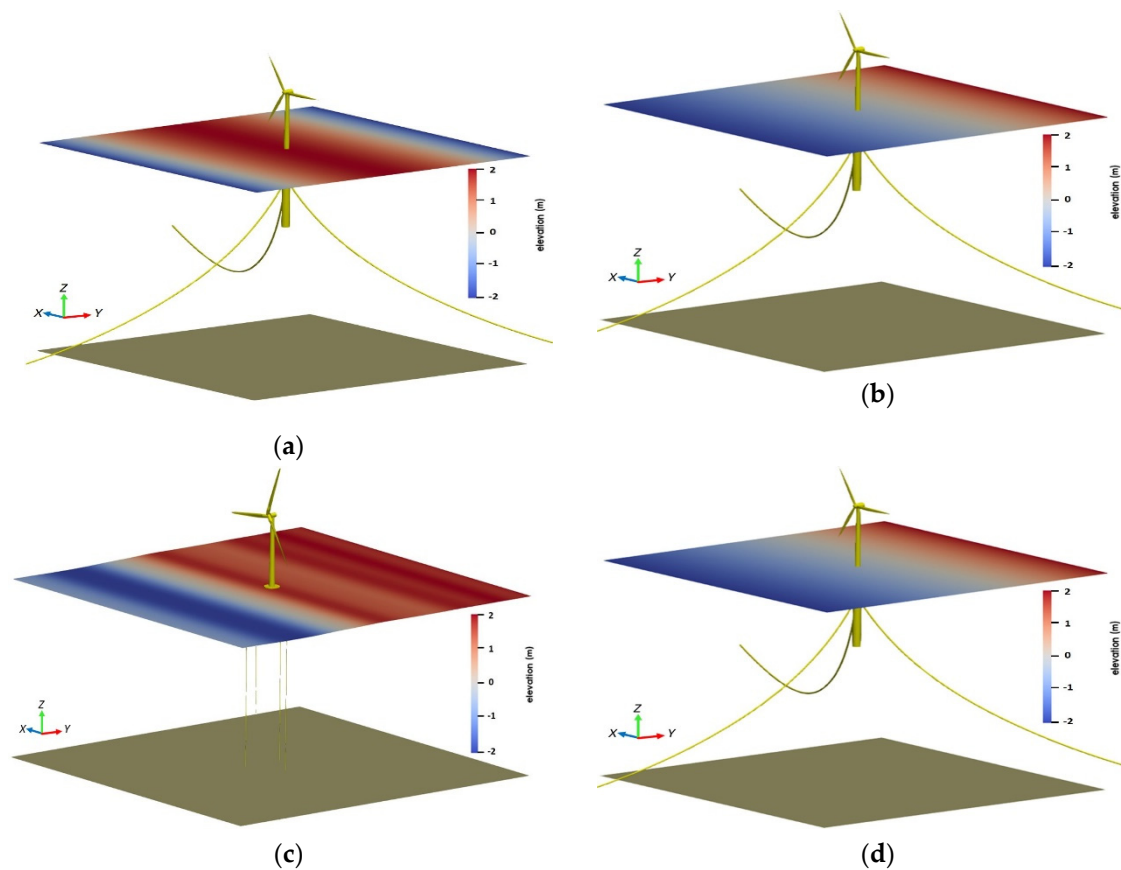


Figure 5. The functions in the modular system.

The software ParaView in the modular system is carried out to visualize the flow field between waves and the floating platform. It is open-source software that can be linked with Python, Matlab, and other programs for multiple data analysis. The objects are able to drawn into a dot map, a grid map, etc., according to the user’s requirements. Meanwhile, the view angle can also be adjusted in the animation by the user. For example, Figure 6a–d present the snapshots of floating OWTs [1], including OC3-Hywind spar, UMaine-Hywind spar, MIT/NREL TLP and UMaine TLP, influenced by the unidirectional irregular waves with respect to free surface elevation, respectively.



**Figure 6.** Snapshots of the unidirectional irregular waves interacting with (a) OC3-Hywind spar; (b) UMaine-Hywind spar; (c) MIT/NREL TLP; and (d) UMaine TLP.

#### 4. Mathematical Model

##### 4.1. Coordinate System

The earth coordinate system  $O_0-X_0Y_0Z_0$ , as indicated in Figure 7, is fixed at  $Z_0 = 0$ , i.e., free surface, with the  $Z_0$ -axis directing upwards and the  $X_0$ -axis denoting wave incidence.  $\omega$  is denoted as the wave angular frequency; wave incident angle  $\theta = 0$  represents waves propagating in the positive  $X_0$  direction;  $h$  is defined as the water depth. The body-fixed coordinate system  $O-XYZ$ , which is able to define the free surface boundary condition, is fixed at COG along with transition or rotation of the floating body.



$$F_i^R \zeta_j = i\rho\omega \iint_s \sum_{j=1}^6 \zeta_j \phi_{Rj} \cdot n_i(x, y, z) dS = \sum_{j=1}^6 (\omega^2 \mu_{ij} + i\omega v_{ij}) \zeta_j, \quad i = 1, 2, \dots, 6 \tag{4}$$

$$\mu_{ij} = -\rho\omega \iint_s \phi_{Rj} \cdot n_i(x, y, z) dS \tag{5}$$

$$v_{ij} = -\rho\omega \iint_s \phi_{Rj} \cdot n_i(x, y, z) dS, \tag{6}$$

where  $F_i^R$  is the  $i$ th mode radiation force.

By adopting the 3D source distribution method,  $\phi_D$  and  $\phi_{Rj}$  can be expressed as:

$$\phi_D(x, y, z) = \iint_s \sigma_D(q) G(p, q) ds \tag{7}$$

$$\phi_{Rj}(x, y, z) = \iint_s \sigma_{Rj}(q) G(p, q) ds, \tag{8}$$

where  $\sigma_D$  and  $\sigma_{Rj}$  represent the source strengths for diffraction and radiation, respectively. Fang and Chen [27] implied that both of these two potentials can be determined by solving the related boundary conditions.

By including the results of wave exciting force, added mass, and radiation damping coefficients, the motion displacements  $\zeta_j$  are obtained via the following six coupled equations of motions:

$$\sum_{j=1}^6 [-\omega^2 (M_{ij} + \mu_{ij}) - i\omega v_{ij} + C_{ij}] \zeta_j = F_i^{ext}, \quad i = 1, 2, \dots, 6, \tag{9}$$

where  $M_{ij}$  is the generalized mass of the floating body, and  $C_{ij}$  the hydrostatic restoring force of the floating body. Finally, the body surface would be divided into numerous panels [19] to solve the velocity potential  $\phi$ .

### 4.3. Cummins Time Domain Equation

The estimation of external forces like wind or wave forces play a major part in determining designs of ships or marine structures. With the force from the mooring connection, the dynamic responses of the floating body are usually calculated by solving motion equations based on the Cummins time domain equation [28], which can be written as below:

$$(M + A_\infty) \ddot{\zeta} = - \int_0^t I(t - \tau) \dot{\zeta}(\tau) d\tau + F_{ext} + F_R + F_B + F_m, \tag{10}$$

where  $A_\infty$  is the added mass matrix at the infinite frequency;  $\ddot{\zeta}$  and  $\dot{\zeta}$  represent the acceleration vector and velocity vector of the floating body in translational or rotational motions, respectively.  $M$  is indicated as the mass matrix;  $I$  the impulse response function;  $F_{ext}$  the wave excitation force;  $F_R$  resultant force from wave radiation in the sinusoidal form, consisting of added-mass force and radiation damping components;  $F_B$  the linear hydrostatic properties of restoring buoyancy force; and  $F_m$  the mooring load.

By using linear quasi-static mooring stiffness, the mooring force  $F_m$  can be represented by

$$F_m = -K_m \zeta - C_m \dot{\zeta}, \tag{11}$$

where  $\zeta$  is defined as the displacement vector of the floating body in the translational or rotational modes.  $K_m$  and  $C_m$  indicate the stiffness and damping matrices of the mooring system.

In order to solve 6-DOF motion responses in the time domain, the Runge-Kutta method is used for numerical simulation. The equation can be written as:

$$u_{i+1} = u_i + \sum_{j=1}^n w_j h k_j, \quad i = 0, 1, 2, \dots, N - 1, \tag{12}$$

where  $u$  is an unknown function of time  $t$ ;  $w_j$  is denoted as the weighting factor;  $h$  the interval size of time  $t$ ;  $k_j$  the increment based on the slope;  $N$  the total data length.

Let the step size  $h > 0$  and define  $n = 4$ ,  $u_{i+1}$  is the approximation of fourth-order Runge-Kutta method and expressed as below:

$$u_{i+1} = u_i + \frac{1}{6} [k_1 + 2k_2 + 2k_3 + k_4], \quad i = 0, 1, 2, \dots, N - 1, \tag{13}$$

where

$$t_{i+1} - t_i = h \tag{14}$$

$$k_1 = hf(t_i, u_i) \tag{15}$$

$$k_2 = hf\left(u_i + \frac{h}{2}, u_i + \frac{1}{2}k_1\right) \tag{16}$$

$$k_3 = hf\left(t_i + \frac{h}{2}, u_i + \frac{1}{2}k_2\right) \tag{17}$$

$$k_4 = hf(t_i + h, u_i + k_3). \tag{18}$$

#### 4.4. Wave Spectrum

In order to generate the wave exciting force in wind-generated seas with a fetch limitation, JONSWAP spectrum [29] can be defined as follows:

$$S(\omega) = \frac{\alpha g^2}{\omega^5} \exp\left[-\frac{5}{4}\left(\frac{\omega_p}{\omega}\right)^4\right] \gamma^\Gamma \tag{19}$$

$$\Gamma = \exp\left[-\frac{(\omega - \omega_p)^2}{2\sigma^2\omega_p^2}\right], \quad \sigma = \begin{cases} 0.07 & \omega \leq \omega_p \\ 0.09 & \omega > \omega_p \end{cases}, \tag{20}$$

where  $\alpha$  is a non-dimensional parameter as a function of the wind speed and fetch length.  $\omega$  is the wave angular frequency, and  $\omega_p$  is the corresponding peak frequency.  $\gamma$  is the peak-enhancement factor, and  $\sigma$  is a relative measure of the width of the peak.

### 5. Analysis of Hydrodynamic Coefficients

The hydrodynamic coefficients of floating OWTs are primarily dominated by the wave exciting force and the radiation force (including added-mass and damping terms), which are usually solved by the potential-flow theory or the Morison equation. The choice of the potential-flow theory or the Morison equation is dependent on the size of the floating platform and the flow field. When the ratio of the diameter of the floating platform to the wave length cannot be neglected, the potential-flow theory would be adopted rather than the Morison equation, and vice versa. More specifically, Morison equation is applicable for calculating the hydrodynamic loads on slender cylinders when (1) the diffraction effects are negligible; (2) radiation damping is negligible; (3) flow separation may occur. The definition of a slender cylinder implies that cylinder diameter,  $D$ , is small relative to the wave length,  $\lambda$ , which is generally met when  $D/\lambda < 0.1-0.2$  in moderate to severe sea states.

In order to acquire convergent hydrodynamic coefficients, the grid-independence test would be carried out for surge, heave and pitch modes, respectively. Accordingly, the wave angular frequency

is set within the range between 0.01 rad/s to 10 rad/s. The wave incidence angle is  $0^\circ$  pointing to the positive  $X_0$ -axis. The ocean current speed, the moving speed of the floating OWTs and the wind speed are neglected in the simulation. The grid-independence tests of hydrodynamic coefficients for four individual floating OWTs are introduced in the following. It is known that the viscous damping induced by the hull drag plays a significant role in calculating hydrodynamic forces of the OC3-Hywind spar or TLPs under the most relevant wave conditions. The other alternative is that the hydrodynamic forces of the floating OWTs can be augmented with additional linear damping, which can be obtained from the free decay test. Although linear damping and viscous damping were not considered in the present hydrodynamic model, the discrepancies of RAOs between our model and other codes would be realized by discussing the damping effect.

5.1. OC3-Hywind Spar/UMaine-Hywind Spar

Since the UMaine-Hywind spar is the same as the OC3-Hywind spar with the exception of the installation water depth, the spar buoy concept with varying mesh discretization would be applied to the grid-independence tests in different water depths. The mesh distribution as shown in Figure 8 can be divided into three parts, i.e., upper column, taper, and base column. The panel properties of the spar buoy for each section are given in Table 2.

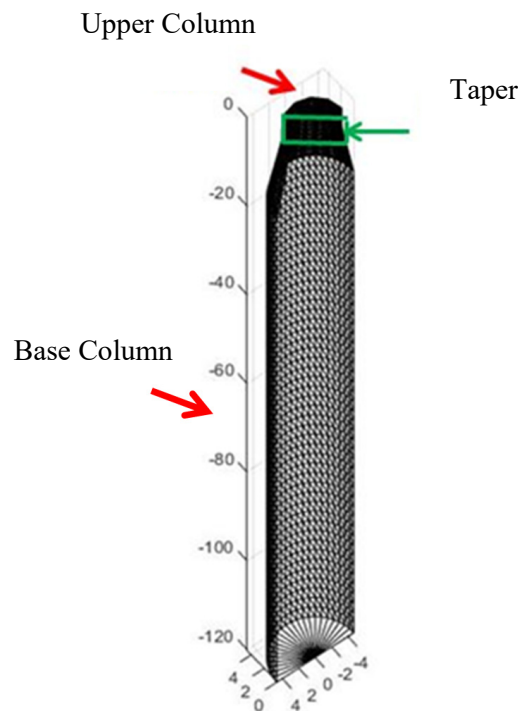


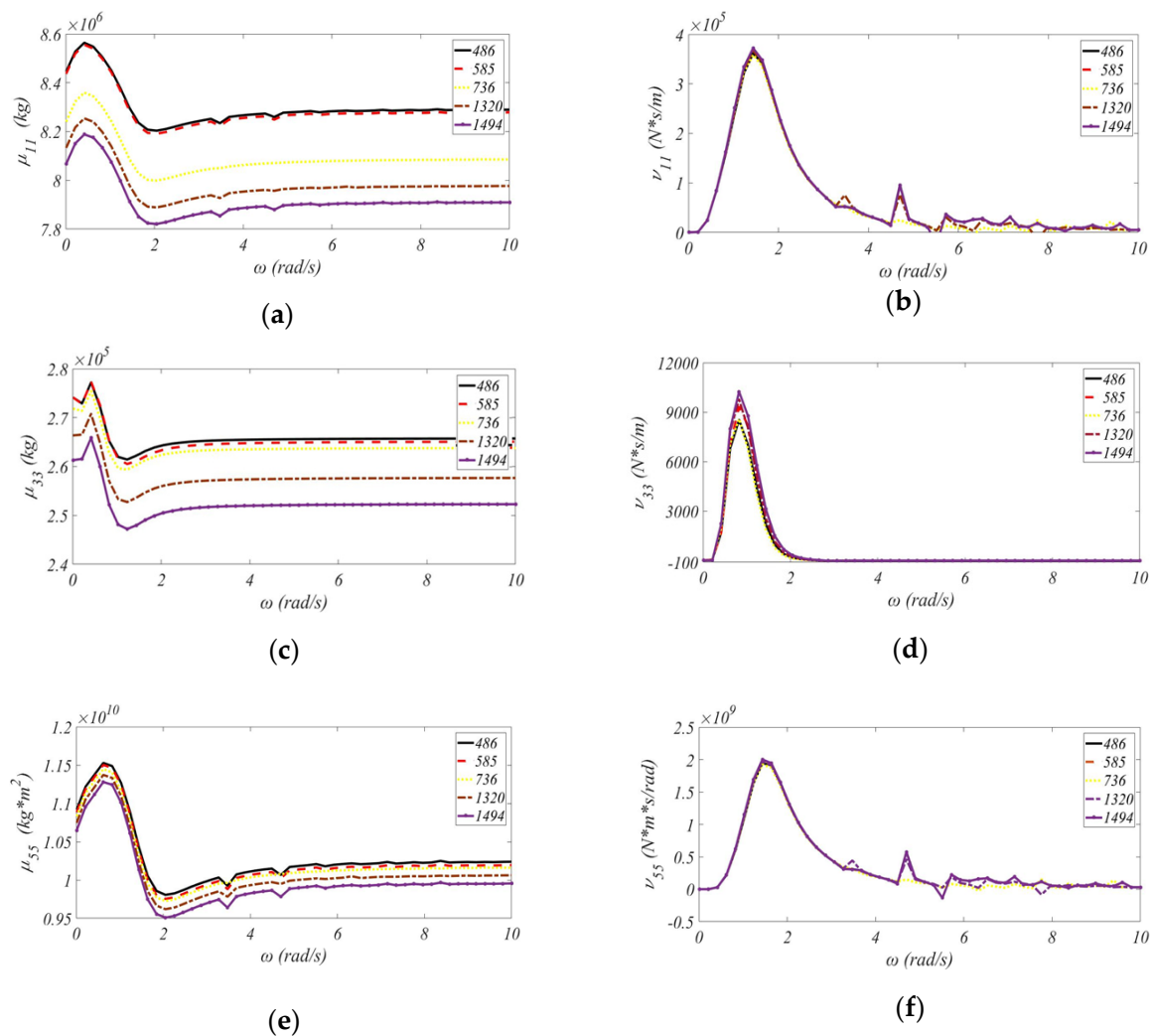
Figure 8. The mesh discretization of the OC3-Hywind spar/UMaine-Hywind spar with triangular panels. (Unit: m).

Table 2. Panel properties of the wetted hull for the OC3-Hywind spar/UMaine-Hywind spar.

	Length/Width (m/m)	Panel Type	Panel Number
Upper Column	1.63/0.33	Triangular	642
Taper	0.86/0.5	Triangular	236
Lower Column	1.72/1	Triangular	442

The properties of added-mass and radiation damping coefficients with different panel numbers in the surge, heave and pitch directions are illustrated in Figure 9a–f for the OC3-Hywind spar and Figure 10a–f for the UMaine-Hywind spar, respectively. Due to the variation in water depth,

it is obvious that the peak values of added-mass coefficients in the pitch mode  $\mu_{55}$  for the OC3-Hywind spar are smaller than those for the UMaine-Hywind spar, whereas the peak values of radiation damping coefficients in the pitch mode  $\nu_{55}$  for the OC3-Hywind spar are larger than those for the UMaine-Hywind spar. By means of the grid independence test, it is exhibited that the difference ratios of 1320 panels and 1494 panels for all hydrodynamic coefficients are less than 1%. Thus, the number of 1320 panels is refined enough for the subsequent simulation of both the OC3-Hywind spar and the UMaine-Hywind spar as shown in the grid-independence test.



**Figure 9.** The mesh convergences for hydrodynamic coefficients (a)  $\mu_{11}$ ; (b)  $\nu_{11}$ ; (c)  $\mu_{33}$ ; (d)  $\nu_{33}$ ; (e)  $\mu_{55}$ ; and (f)  $\nu_{55}$  of wetted hull for the OC3-Hywind spar under different panel numbers.

In addition, the aspect ratios of triangular panels for upper column, taper and base column of the spar buoy are set to 1.63/0.33 for 642 panels, 0.86/0.5 for 236, and 1.72/1 for 442 panels, respectively. Eventually, all panels can be grouped into three families of the same size and proportion by panel clustering.

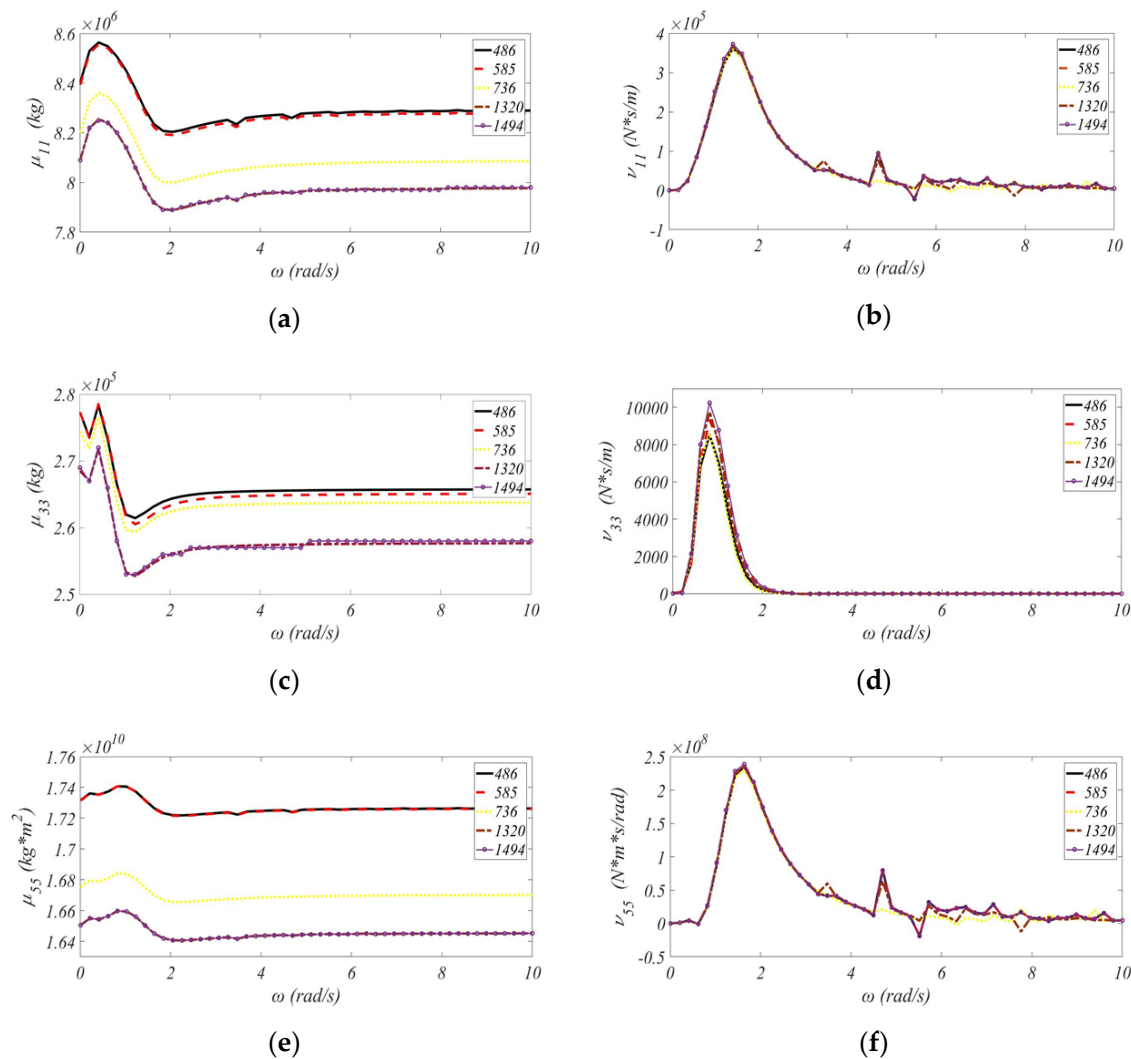


**Figure 10.** The mesh convergences for hydrodynamic coefficients (a)  $\mu_{11}$ ; (b)  $\nu_{11}$ ; (c)  $\mu_{33}$ ; (d)  $\nu_{33}$ ; (e)  $\mu_{55}$ ; and (f)  $\nu_{55}$  of wetted hull for the UMaine-Hywind spar under different panel numbers.

### 5.2. MIT/NREL TLP

The mesh discretization of the MIT/NREL TLP wetted hull with triangular panels is illustrated in Figure 11. Since the MIT/NREL TLP features one center column with four pontoons, the panel properties for each structure are introduced in Table 3.

The properties of added-mass and radiation damping coefficients with different panel numbers in the surge, heave and pitch directions are illustrated in Figure 12a–f, respectively. Generally, it is found that the peak values of these two hydrodynamic coefficients are occurred around 1.7 rad/s. The values of added-mass coefficients  $\mu_{11}$  and  $\mu_{55}$  are significantly greater than the one  $\mu_{33}$  because the displaced water and the wetted surface in the surge and pitch modes are larger than those in the heave mode. The radiation damping coefficients vanish at both of the low- and high-frequency limits of the wind-generated wave spectrum (from 1 to 30 s), indicating that the radiation damping is increased in the normal sea states.

**Table 3.** Panel properties of the MIT/NREL TLP wetted hull.

	Length/Width (m/m)	Panel Type	Number of Panels
Center Column	2.92/2.81	Triangular	1163
Pontoon	2/0.54	Triangular	843

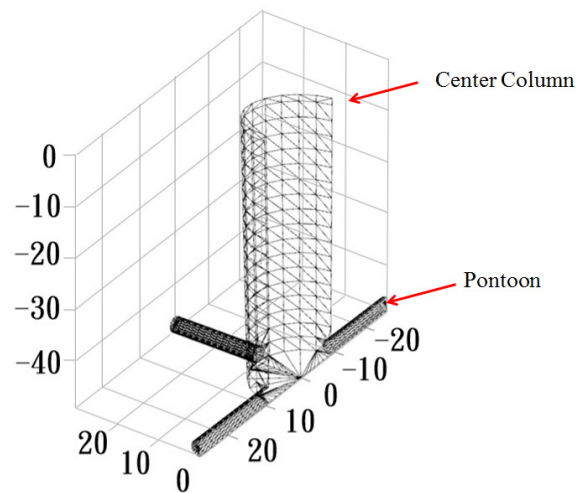


Figure 11. The mesh discretization of the MIT/NREL TLP with triangular panels. (Unit: m).

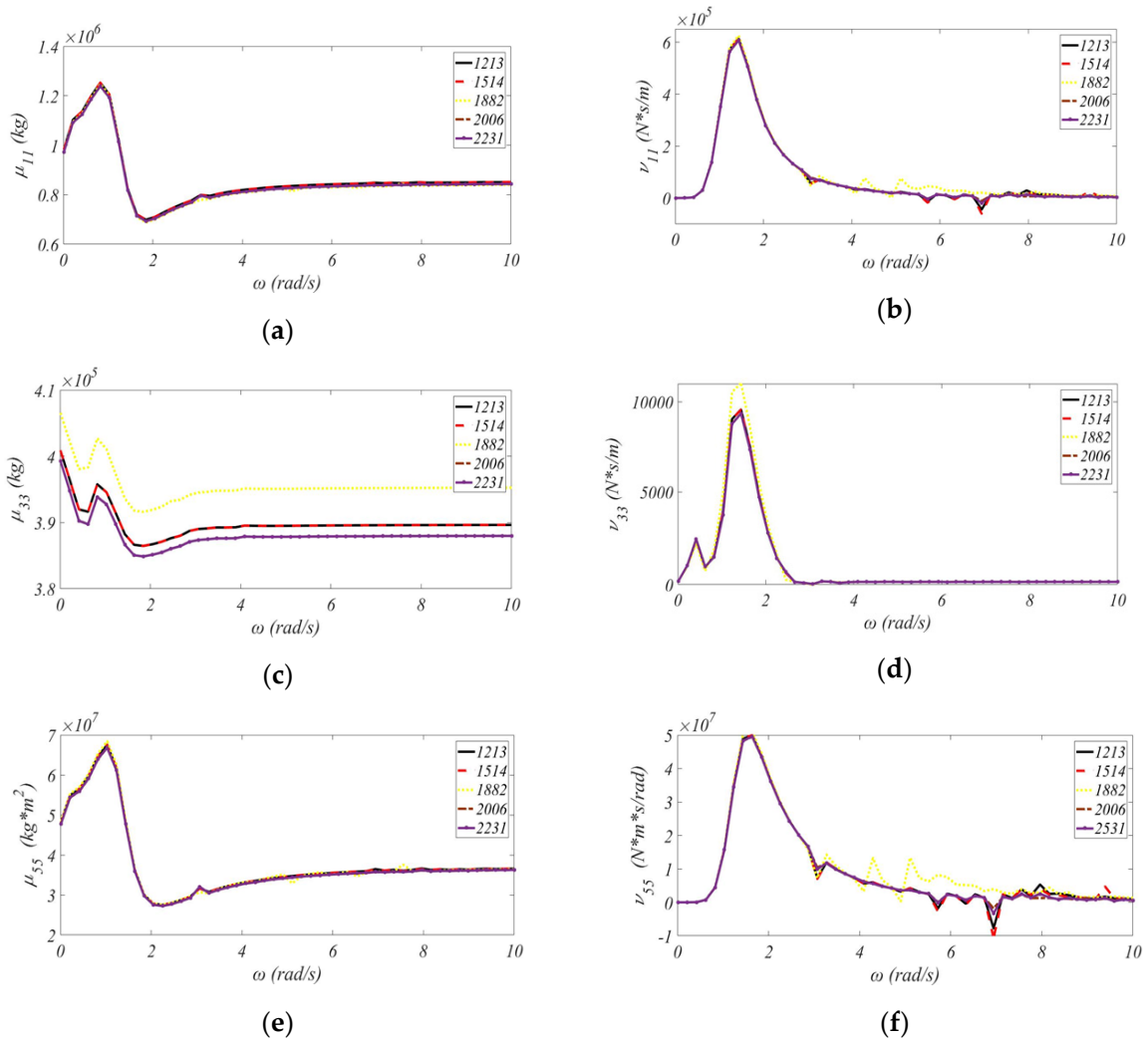


Figure 12. The mesh convergences for hydrodynamic coefficients (a)  $\mu_{11}$ ; (b)  $\nu_{11}$ ; (c)  $\mu_{33}$ ; (d)  $\nu_{33}$ ; (e)  $\mu_{55}$ ; and (f)  $\nu_{55}$  of the NREL/MIT TLP wetted hull under different panel numbers.

The grid-independence test reaches convergence if there is a small difference between two adjacent refinements. Except for 1882 panels, the mesh convergence basically improves monotonously with the number of panels. The discrepancy occurs due to the fact that the panels might not be distributed

uniformly. Consequently, the results indicate that the difference ratios of 2006 panels and 2231 panels for all hydrodynamic coefficients are less than 1%. Thus, the number of 2006 panels is refined enough for the subsequent simulation of the MIT/NREL TLP as shown in the grid-independence test. Furthermore, the aspect ratios of triangular panels for center column and pontoons are set to be 2.92/2.81 for 1163 panels and 2/0.54 for 843 panels, respectively. Consequently, all panels can be grouped into two families of the same size and proportion by panel clustering.

### 5.3. UMaine TLP

The mesh discretization of the UMaine TLP wetted hull with triangular panels is presented in Figure 13. The UMaine TLP features an upper hull over a lower hull connected with four tendon arms. The panel properties for each structure are introduced in Table 4.

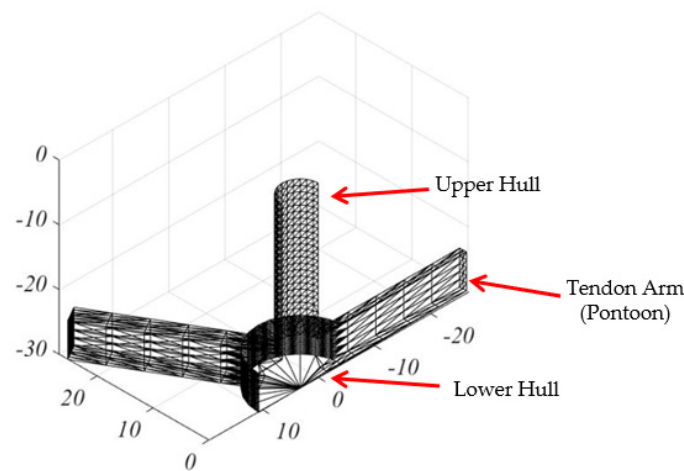


Figure 13. The mesh discretization of the UMaine TLP with triangular panels. (Unit: m.)

Table 4. Panel properties of the UMaine TLP wetted hull.

	Length/Width (m/m)	Panel Type	Panel Number
Upper Hull	0.79/1	Triangular	648
Lower Hull	2/0.25	Triangular	332
Tendon Arm (Pontoon)	5/0.6	Triangular	340

The properties of added-mass and radiation damping coefficients with different panel numbers in the surge, heave, and pitch directions are illustrated in Figure 14a–f, respectively. It is shown that the peak values of these two hydrodynamic coefficients are occurred at different locations in surge, heave and pitch directions. The difference of added-mass coefficients  $\mu_{11}$  and  $\mu_{33}$  for the UMaine TLP is less than the one for the MIT/NREL TLP because the displaced water and the wetted surface in the surge mode are only slightly larger than those in the heave mode. Since the radius and diameter of the pontoon for the UMaine TLP are larger than the ones for the MIT/NREL TLP, the value of added-mass coefficient in the pitch mode  $\mu_{55}$  is found to be considerably larger than the results in the heave and pitch modes. The increases in the radius and diameter of the pontoon shift the resonance peak of the radiation damping coefficient in the surge mode to the high frequency, whereas the decrease in the diameter of the column shortens the resonance peak frequency of the radiation damping coefficient in the heave mode.

By means of the grid-independence test shown in Figure 14c, it is exhibited that the difference ratios of 1322 panels and 1834 is caused by the mesh distribution over different parts of UMaine TLP. However, the convergence is considered to be reached because the difference ratios of 1322 panels and

1834 panels for all hydrodynamic coefficients are still less than 1%. Thus, the number of 1322 panels is refined enough for the subsequent simulation of the UMaine TLP as shown in the grid-independence test. In addition, the aspect ratios of triangular panels for upper hull, lower hull and tendon arms are set to be 0.79/1 for 648 panels, 2/0.25 for 332 panels, and 5/0.6 for 340 panels, respectively. Eventually, all panels can be grouped into three families of the same size and proportion by panel clustering. By considering the same underwater meshes for OC3-Hywind and UMaine-Hywind spars in different water depths, it is found that the water depth does interfere with the hydrodynamic coefficients in the heave and pitch modes due to the boundary effect.

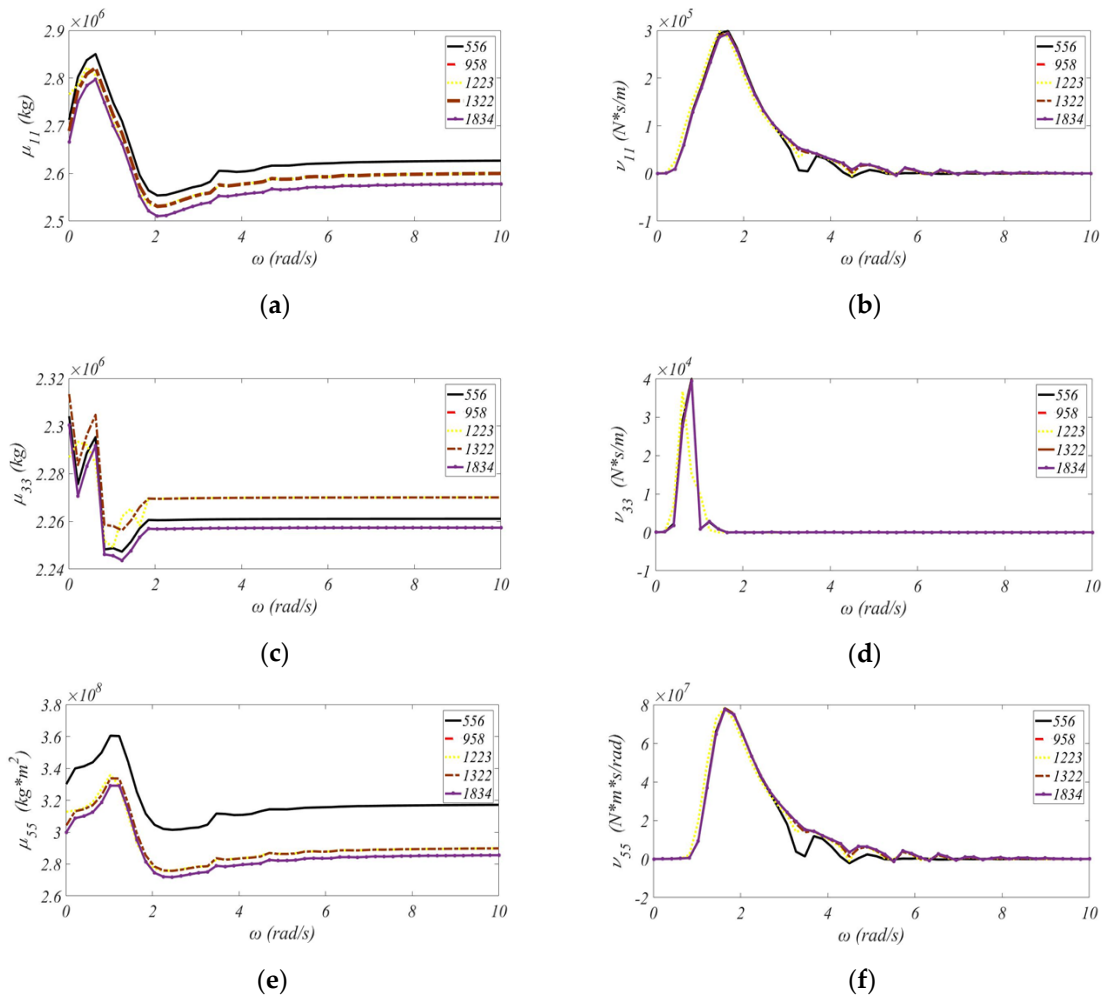


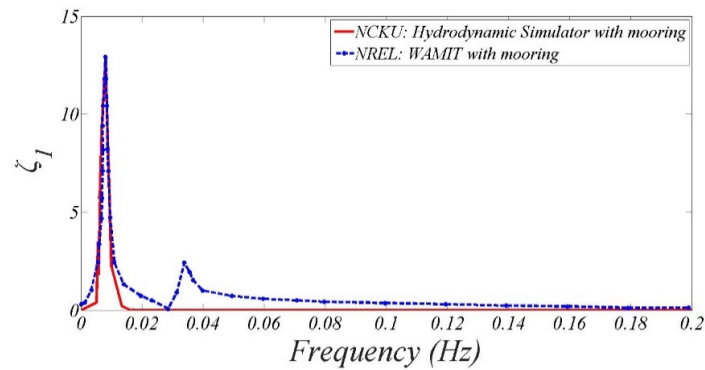
**Figure 14.** The mesh convergences for hydrodynamic coefficients (a)  $\mu_{11}$ ; (b)  $\nu_{11}$ ; (c)  $\mu_{33}$ ; (d)  $\nu_{33}$ ; (e)  $\mu_{55}$ ; and (f)  $\nu_{55}$  of the UMaine TLP wetted hull under different panel numbers.

## 6. Dynamic Responses of Floating OWTs

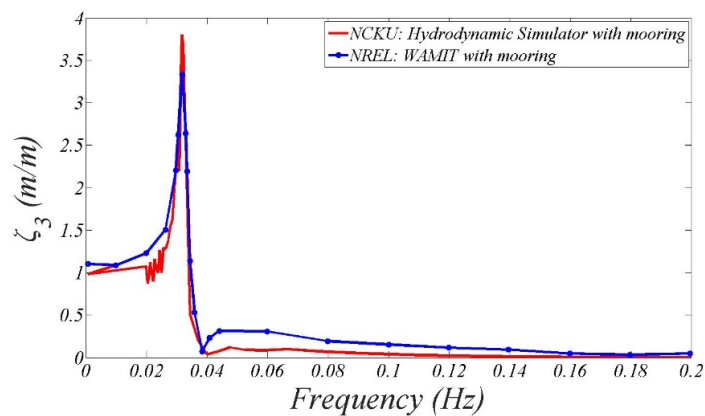
After analyzing hydrodynamic coefficients of floating OWTs, the Response Amplitude Operators (RAOs) would be applied to three typical motion responses, i.e., surge, heave, and pitch. In addition, the performances of floater’s dynamics were compared with other published data. It is noted that the coupling motion responses were not considered in the present study. In order to analyze the characteristics of wave-load components once the mooring load is added, time histories of wave-load components at the natural frequencies of surge, heave and pitch for each floating OWT would be presented in the following sections.

### 6.1. OC3-Hywind Spar

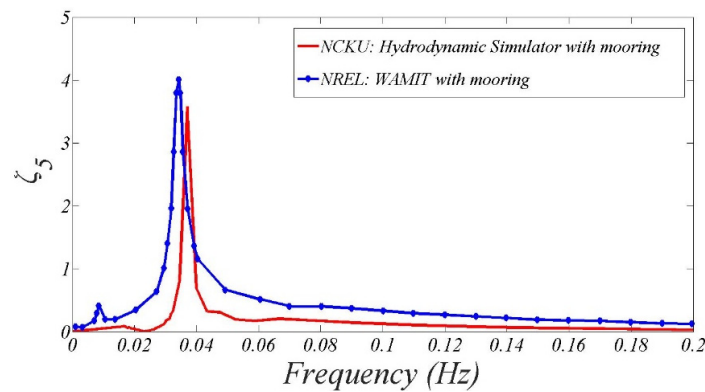
Since the RAOs appear considerable excitation in the surge, heave and pitch modes among all 6-DOF motions [30], only these three RAOs computed by using hydrodynamic simulator and WAMIT [31], which is based on the linear and second-order potential theory, with a series of regular waves ( $H_0 = 5$  m,  $T_0 = 2.5 \sim 20$  s) are compared for the OC3-Hywind spar, as shown in Figure 15a–c, respectively. Although a small frequency shift is occurred for the pitch response at the natural frequency, the computed RAOs with mooring loads from hydrodynamic simulator agree well with the results predicted by WAMIT.



(a)



(b)

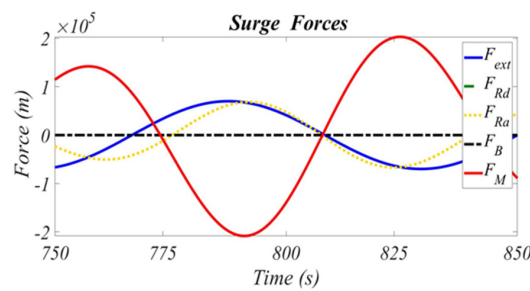


(c)

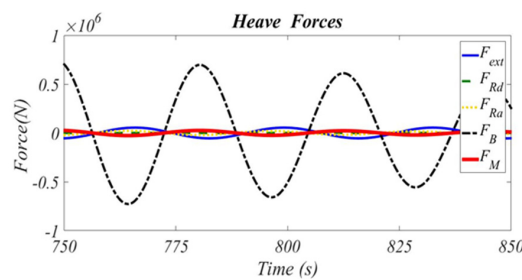
**Figure 15.** The performance of (a) surge, (b) heave, and (c) pitch RAOs as a function of wave frequency for the OC3-Hywind spar by comparing hydrodynamic simulator with WAMIT.

In Figure 15a, the surge RAO predicted by using hydrodynamic simulator with the mooring load is smaller than the one predicted by WAMIT in the high-frequency region because the mooring load is overestimated in absence of the damping matrix of the mooring system. For the case with the mooring effect, there is a resonance peak at the natural frequency ( $f_p = 0.008$  Hz) in the surge mode. Although it is not shown here, the numerical simulation indicates that the mooring load has the effect on the RAO as well as the natural frequency. It is exhibited in Figure 15b that the discrepancy of the heave RAO between WAMIT and our numerical simulation is small. Meanwhile, the OC3-Hywind spar basically follows the wave in heave for an extremely low-frequency wave. In case of the mooring effect, the frequency shift of the resonance peak in pitch RAO between hydrodynamic simulator and WAMIT as shown in Figure 15c could be due to a slight stiffening of the catenary mooring lines in the WAMIT simulation. In our mooring load equation, the mooring force was calculated by using linear quasi-static mooring stiffness. For simplifying the numerical computation, the elements in the damping matrix of the mooring system are all set to zero. Therefore, the mooring effect on the pitch motion could be overestimated.

Figure 16a–c exhibit time variations of wave exciting force ( $F_{ext}$ )/moment ( $M_{ext}$ ), radiation damping force ( $F_{Rd}$ )/moment ( $M_{Rd}$ ), radiation added-mass force ( $F_{Ra}$ )/moment ( $M_{Ra}$ ), buoyancy force ( $F_B$ )/moment ( $M_B$ ) and mooring force ( $F_M$ )/moment ( $M_M$ ) at the natural frequencies of the surge, heave and pitch, respectively. The input wave condition for calculating the force at the natural frequency of each mode is a regular wave  $H_0 = 5$  m and  $T_0 = T_n$  ( $T_n$ : Natural period). The phase lags in time histories of wave-load components indicate the relationships between the wave exciting force and other wave-load components. It is obvious in Figure 16a that  $F_M$  is the most superior force at the surge natural frequency among all wave-load components, which is able to explain the contribution of the mooring load to the surge RAO in Figure 15a. However, it is noted that the quasi-static mooring force could be overestimated when ignoring the damping effect of the mooring system. This adequately explains why the mooring force is greater than the wave exciting force in the surge mode. It is found in Figure 16(b) that  $F_M$  has less influence on the dynamic response of the OC3-Hywind spar at the heave natural frequency. However,  $F_B$  is the dominant force at the heave natural frequency due to deeply draft of the slender body. Figure 16c indicates that  $M_{ext}$  plays the most significant part at the pitch natural frequency, which is mainly attributed to the large pitch inertia about CM.



(a)



(b)

Figure 16. Cont.

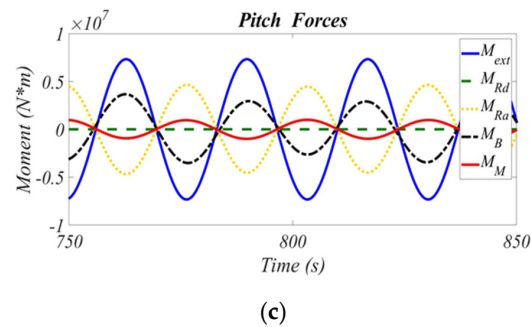


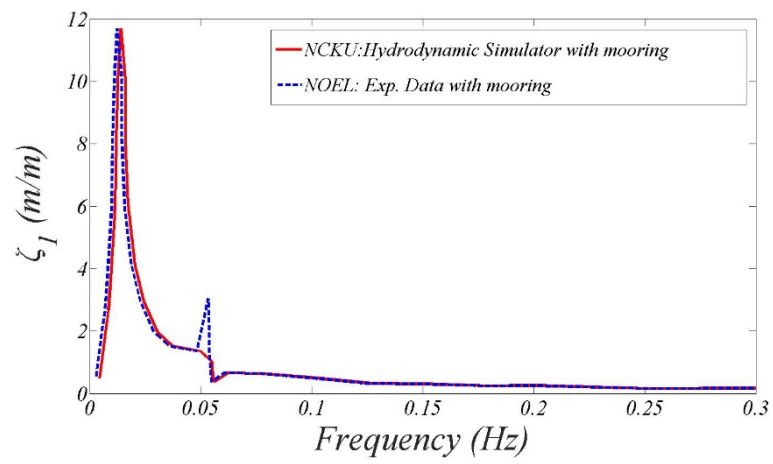
**Figure 16.** Time histories of wave-load components at (a) the surge natural frequency ( $f_p = 0.008$  Hz), (b) the heave natural frequency ( $f_p = 0.032$  Hz), and (c) the pitch natural frequency ( $f_p = 0.037$  Hz) for the OC3-Hywind spar.

## 6.2. UMaine-Hywind Spar

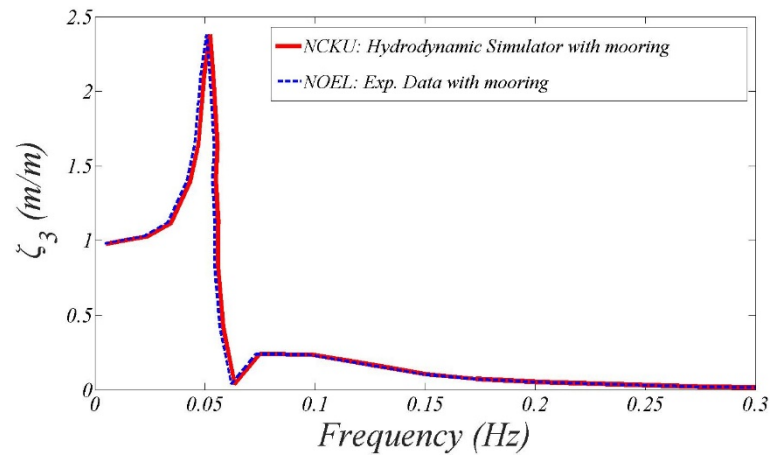
Figure 17a–c show the comparisons of RAOs at surge, heave and pitch natural frequencies between hydrodynamic simulator and the experimental data from a 1:30 model implemented in Natural Ocean Engineering Laboratory (NOEL) of Reggio Calabria in Italy [32,33]. The given wave condition adopted for dynamic response of MIT/NREL spar is JONSWAP spectrum ( $H_s = 6$  m,  $T_p = 10$  s, and peak-enhancement factor:  $\gamma = 3.3$ ). Since the UMaine-Hywind spar is at 200 m of the water depth shallower than the OC3-Hywind spar at 320 m, the length of the catenary mooring lines resting on the seabed are shorter than that used for the OC3-Hywind spar. That means the stiffness of the catenary mooring lines used for the UMaine-Hywind spar is higher than that used for the OC3-Hywind spar. Consequently, the peak value of the surge with the mooring load computed by hydrodynamic simulator as shown in Figure 17a is smaller than the case in Figure 15a because of high stiffening of mooring lines in the surge mode. It is exhibited that the resonance peak of the heave RAO with the mooring load in Figure 17b is also smaller than the one in Figure 15b due to the effect of shallow water depth. However, decreases in the water depth would lead to more prominent resonance peaks of pitch RAOs in Figure 17c than the ones in Figure 15c.

According to the Boundary Element Method (BEM) [34], proximity to a boundary can have the influence on the quantity of hydrodynamic coefficients. This means that added-mass and radiation damping coefficients not only depend on the floater's geometry but also its proximity to a boundary. For floating bodies, the response of the floating body is altered in finite water depth. The specific water depth at which the hydrodynamic coefficient is affected depends on the floater's geometry, location and shape of a boundary, e.g., the seabed. Therefore, the water depth may have the effects on the RAOs for OC3- and UMaine-Hywind spars.

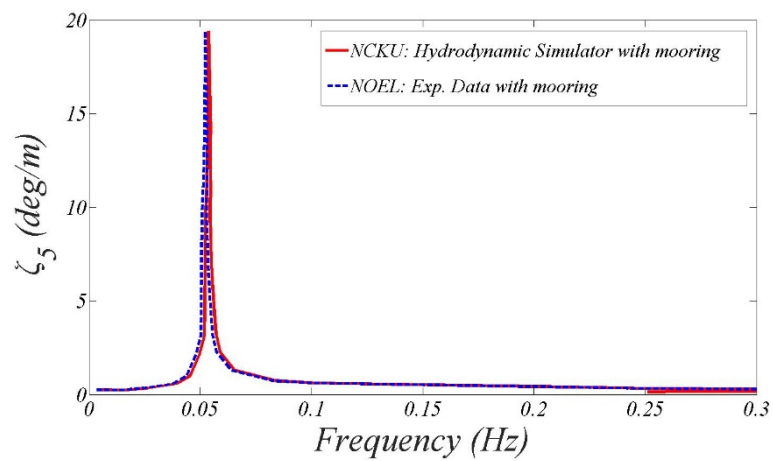
Figure 18a–c present time variations of wave load components at the natural frequencies of the surge, heave and pitch, respectively. Compared with the dominant force of  $F_B$  in Figure 16b, it is evident in Figure 18b that  $F_B$  is even more significant at the heave natural frequency with the increase of the significant wave height.



(a)

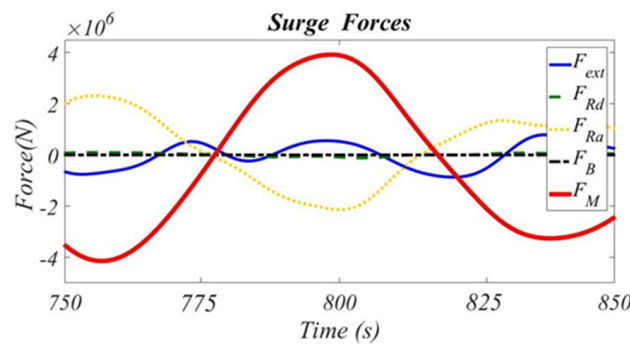


(b)

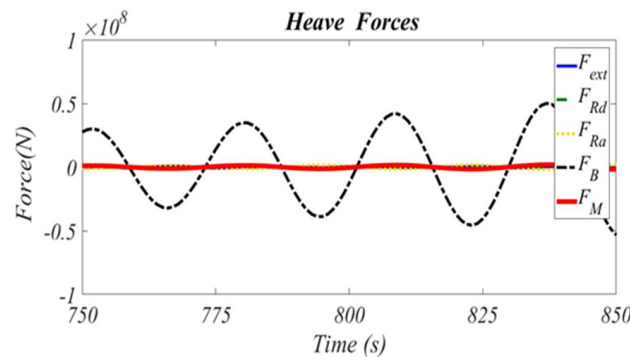


(c)

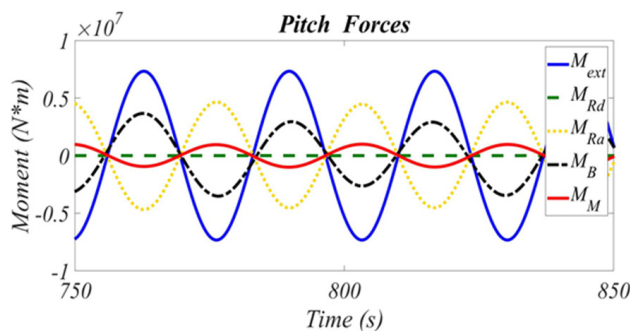
**Figure 17.** The performance of (a) surge, (b) heave, and (c) pitch RAOs as a function of wave frequency for the UMaine-Hywind spar by comparing hydrodynamic simulator with experimental data of NOEL.



(a)



(b)



(c)

**Figure 18.** Time histories of wave-load components at (a) the surge natural frequency ( $f_p = 0.014$  Hz), (b) the heave natural frequency ( $f_p = 0.052$  Hz), and (c) the pitch natural frequency ( $f_p = 0.054$  Hz) for the UMaine-Hywind spar.

### 6.3. MIT/NREL TLP

The given wave condition adopted for dynamic response of MIT/NREL TLP is JONSWAP spectrum (significant wave height:  $H_s = 5$  m, peak period:  $T_p = 8.7$  s, and peak-enhancement factor:  $\gamma = 2.4$ ). As illustrated in Figure 19a,b, The RAO analysis of surge and heave with the mooring load conducted by the hydrodynamic simulator will be in comparison with the results from NREL design code, Fatigue, Aerodynamics, Structures, and Turbulence (FAST), executed by Shim and Kim [35]. FAST is NREL’s primary CAE tool, enabling coupled nonlinear aero-hydro-servo-elastic simulation of wind turbines in the time domain. It is clearly shown that the surge RAO is considerably larger than the heave RAO because the mooring system is much stiff in the vertical plane. Although second-order mean drift forces are considered to simulate slowly varying horizontal-plane drift motions through Newman’s approximation method in their study, our results are generally in good agreement with FAST’s results except for a slight shift of the peak in the surge RAO. Furthermore, Tracy [36] indicated

that the TLP represents the most attractive option as a result of its low Root Mean Square (RMS) accelerations and negligible heave and pitch motions.

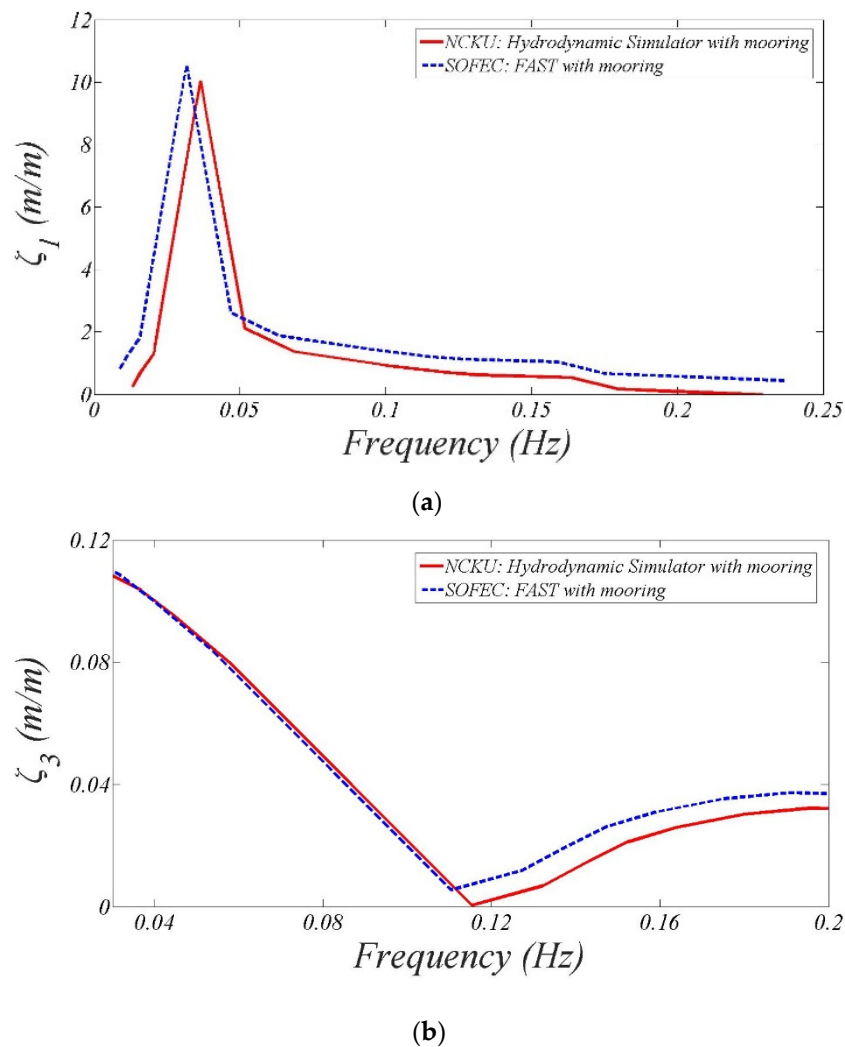


**Figure 19.** The performance of (a) surge and (b) heave RAOs as a function of wave frequency for the MIT/NREL TLP by comparing hydrodynamic simulator with FAST.

The time histories in Figure 20a,b show that the surge oscillation excites individual wave-load components by couplings with the taut-leg mooring system to oscillations at the surge and heave natural frequencies, respectively. It is obvious that the mooring load has a greater contribution to motion restriction of the MIT/NREL TLP at the heave natural frequency than that at the surge natural frequency. For taut lines of a TLP with no part of the cables lying on the seabed, the linearity assumption of the stiffness matrix is a relatively good approximation to vertical forces.

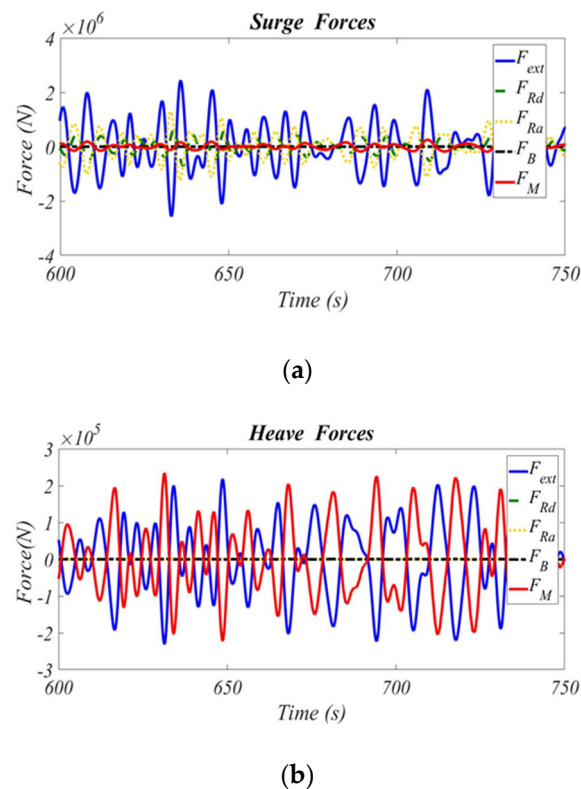
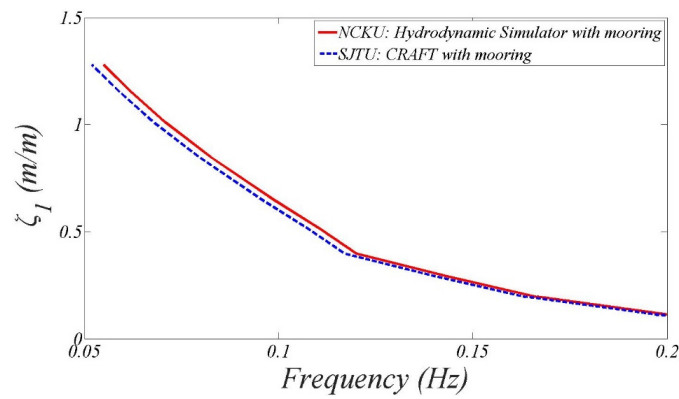


**Figure 20.** Time histories of wave-load components at (a) the surge natural frequency ( $f_p = 0.037$  Hz), and (b) the heave natural frequency ( $f_p = 0.015$  Hz) for the MIT/NREL TLP.

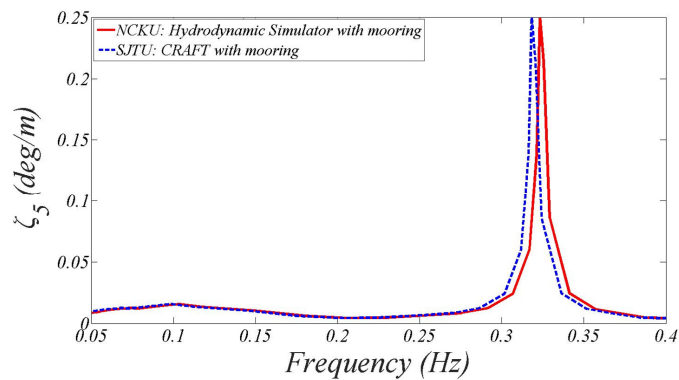
#### 6.4. UMaine TLP

Since the surge and pitch motions could be the most two dominant modes of the dynamic responses of the UMaine TLP, a series of regular wave cases ( $H_0 = 5$  m,  $T_0 = 2.5 \sim 20$  sec) are implemented to capture the response characteristics of these two motions by comparing hydrodynamic simulator with CRAFT (Coupled Response Analysis of Floating wind Turbine) [3]. CRAFT accounts for the nonlinear tendon dynamics and viscous drag force imposed on the horizontal pontoons. As shown in Figure 21a,b, the surge and pitch RAOs obtained from these two codes are comparable and consistent with each other. Specifically, it is evident in Figure 21a that the influence of the second-order drift force could be insignificant because the excitations and motions of the surge RAO are small. Figure 21b exhibits that the pitch resonant frequency (0.323 Hz) predicted by hydrodynamic simulator is very close to the result (0.319 Hz) obtained from FAST. The peak value predicted by hydrodynamic simulator is also very close to the one predicted using FAST, but a small discrepancy is caused by the damping effect of the viscous drag force on the main column and pontoons.

It is clearly shown in Figure 22a that the wave load is mainly dominated by the wave exciting force and radiation added-mass force at the surge natural frequency because of their large cross-sectional areas of the pontoons in the surge mode. The effect of the taut-leg mooring system on the dynamic responses as illustrated in Figure 22b is relatively evident at the pitch natural frequency than that at the surge natural frequency. It appears that the taut-leg mooring system has an increasing dominant effect on the pitch motion, but has a decreasing effect on the surge motion for increasing wave frequencies.

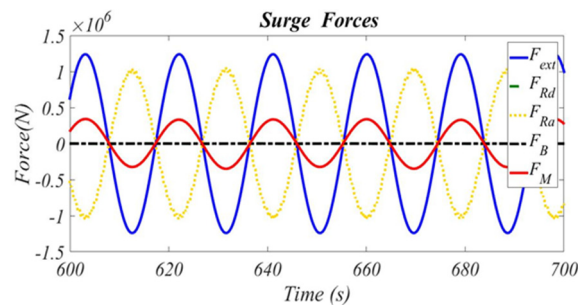


(a)

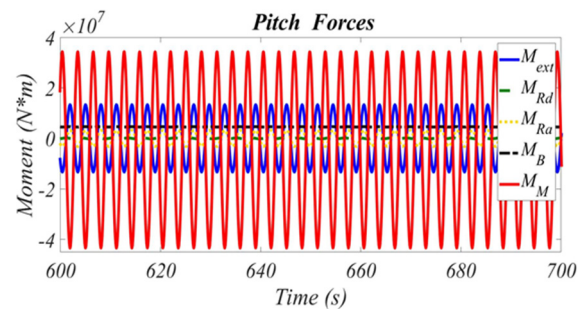


(b)

**Figure 21.** The performance of (a) surge, and (b) pitch RAOs as a function of wave frequency for the UMaine TLP by comparing hydrodynamic simulator with FAST.



(a)



(b)

**Figure 22.** Time histories of wave-load components at (a) the surge natural frequency ( $f_p = 0.053$  Hz), and (b) the pitch natural frequency ( $f_p = 0.323$  Hz) for the UMaine TLP.

## 7. Conclusions

This study intends to develop a modularized simulation system to resolve hydrodynamic coefficients as well as motion responses of surge, heave, and pitch for the floating OWTs based on the concepts of spar buoy and TLP. The capability of the modularized simulation system has been examined by comparing the simulation results with those predicted using other codes as well as with experimental data. The following summaries by including the mooring effect would be described from the simulation results.

1. For the spar buoy concept, the decrease in water depth results in larger added-mass coefficient in the pitch mode  $\mu_{55}$ , but causes smaller radiation damping coefficient in the pitch mode  $\nu_{55}$ .
2. For the design of the MIT/NREL TLP, the larger displaced water and the wetted surface in the surge and pitch modes would lead to higher added-mass coefficients  $\mu_{11}$  and  $\mu_{55}$  than the value in the heave mode  $\mu_{33}$ .
3. Compared to the design of the MIT/NREL TLP, the large radius and diameter of the pontoon for the UMaine TLP would produce high value of the added-mass coefficient in the pitch mode  $\mu_{55}$ . The increases in the radius and diameter of the pontoon are accompanied with low resonance frequency of the radiation damping coefficient in the surge mode, whereas the decrease in the diameter of the column is related to low resonance frequency of the heave coefficient.
4. Due to the influence of unstretched mooring lines parallel to the seabed on the OC3-Hywind spar, the catenary mooring system has considerable contribution to the surge RAO, but provides for less effect on the heave RAO.
5. From the computed results of UMaine-Hywind spar in irregular seas, the decrease in the water depth would lead to more prominent resonance peaks of pitch RAOs and also shift the peaks to the high-frequency region as a result of proximity to the seabed.
6. It is demonstrated in this paper that the surge RAO is considerably larger than heave and pitch RAOs for the TLP concept due to high stiffening in the vertical plane of the taut-leg mooring system. Specifically, the large cross-sectional areas of the pontoons for the UMaine TLP would produce larger radiation added-mass force in the surge mode than in the pitch mode.
7. Concerning the floater's stability in severe sea conditions, it is much suitable to install the spar buoy in deep water area when neglecting the cost of the mooring system. For the TLP option, it is better to consider UMaine TLP rather than MIT/NREL TLP because the surge RAO can be well suppressed.

**Author Contributions:** Formal analysis, S.-H.K.; Investigation, C.-H.Y.; Methodology, Y.-H.L.; Supervision, Y.-H.L.; Writing—original draft, Y.-H.L.

**Acknowledgments:** The authors would like to express their thanks to the Ministry of Science and Technology for a grant under Contract No. MOST 107-2221-E-006-229. The authors also acknowledge the support provided by the College of Engineering, National Cheng Kung University.

**Conflicts of Interest:** The authors declare no conflict of interest.

## References

1. Robertson, A.N.; Jonkman, J.M. Loads analysis of several offshore floating wind turbine concepts. In Proceedings of the Twenty-First International Offshore and Polar Engineering Conference: International Society of Offshore and Polar Engineers, Maui, HI, USA, 19–24 June 2011.
2. Statoil. *Hywind by Statoil: The Floating Wind Turbine*; Statoil: Stavanger, Norway, 2012.
3. Shen, M.C.; Hu, Z.G.; Liu, G.L. Dynamic response and viscous effect analysis of a TLP-type floating wind turbine using a coupled aero-hydro-mooring dynamic code. *Renew. Energy* **2016**, *99*, 800–812. [[CrossRef](#)]
4. Bachynski, E.E.; Moan, T. Design considerations for tension leg platform wind turbines. *Mar. Struct.* **2012**, *29*, 89–114. [[CrossRef](#)]
5. DNV-GL. Design of floating wind turbine structures. *Offshore Standard DNV-OS-J103* **2013**, *5*, 1–124.

6. Tran, T.T.; Kim, D.H. Fully coupled aero-hydrodynamic analysis of a semi-submersible FOWT using a dynamic fluid body interaction approach. *Renew. Energy* **2016**, *92*, 244–261. [[CrossRef](#)]
7. Liu, Y.C.; Xiao, Q.; Incecik, A.; Peyrard, C.; Wan, D.C. Establishing a fully coupled CFD analysis tool for floating offshore wind turbines. *Renew. Energy* **2017**, *112*, 280–301. [[CrossRef](#)]
8. Butterfield, S.; Musial, W.; Jonkman, J.; Sclavounos, P. *Engineering Challenges for Floating Offshore Wind Turbines*; National Renewable Energy Laboratory (NREL): Golden, CO, USA, 2007.
9. James, R.; Ros, M.C. *Floating Offshore Wind: Market and Technology Review*; Carbon Trust UK: London, UK, 2015; p. 168.
10. Chen, Z.-Z.; Tarp-Johansen, N.J.; Jensen, J.J. Mechanical characteristics of some deepwater floater designs for offshore wind turbines. *Wind Eng.* **2006**, *30*, 417–430. [[CrossRef](#)]
11. Al-Solihat, M.K.; Nahon, M. Stiffness of slack and taut moorings. *Ships Offshore Struct.* **2016**, *11*, 890–904. [[CrossRef](#)]
12. Matha, D. *Model Development and Loads Analysis of an Offshore Wind Turbine on a Tension Leg Platform with a Comparison to Other Floating Turbine Concepts: April 2009*; National Renewable Energy Laboratory (NREL): Golden, CO, USA, 2010.
13. Karimirad, M.; Moan, T. Wave-and wind-induced dynamic response of a spar-type offshore wind turbine. *J. Waterw. Port Coast. Ocean Eng.* **2011**, *138*, 9–20. [[CrossRef](#)]
14. Amo, O.M.; Fossen, T.I. Finite element modelling of moored vessels. *Math Comp. Model Dyn.* **2001**, *7*, 47–75. [[CrossRef](#)]
15. Hooke, R.; Jeeves, T.A. Direct search solution of numerical and statistical problems. *J. Assoc. Comput. Mach.* **1961**, *8*, 212–229. [[CrossRef](#)]
16. Korvin-Kroukovsky, B.V.; Jacobs, W.R. *Pitching and Heaving Motions of a Ship in Regular Waves*; Stevens Institute of Technology: Hoboken, NJ, USA, 1957.
17. Fang, M.-C.; Chen, T.-Y. A parametric study of wave loads on trimaran ships traveling in waves. *Ocean Eng.* **2008**, *35*, 749–762. [[CrossRef](#)]
18. Lin, Y.-H.; Hsu, C.-L.; Kao, S.-H. Hydrodynamics of the wind float OC3-Hywind with mooring loads estimated by the modular system. *J. Mar. Sci. Technol.* **2018**, 1–12. [[CrossRef](#)]
19. Hess, J.L.; Smith, A. *Calculation of Non-Lifting Potential Flow about Arbitrary Three-Dimensional Bodies*; Douglas Aircraft Co: Long Beach, CA, USA, 1962.
20. Shen, H.-T.; Farrell, C. Numerical calculation of the wave integrals in the linearized theory of water waves. *J. Ship Res.* **1975**, *21*, 1–10.
21. Telste, J.; Noblesse, F. Numerical evaluation of the Green function of water-wave radiation and diffraction. *J. Ship Res.* **1986**, *30*, 69–84.
22. Salvesen, N.; Tuck, E.; Faltinsen, O. Ship motions and sea loads. *Trans. SNAME* **1970**, *78*, 250–287.
23. ETAP\_Balkan. *Wind Turbine Modeling*; ETAP\_Balkan: Istanbul, Turkey, 2018.
24. Andersen, M.T.; Hindhede, D.; Lauridsen, J. Influence of model simplifications excitation force in surge for a floating foundation for offshore wind turbines. *Energies* **2015**, *8*, 3212–3224. [[CrossRef](#)]
25. Jonkman, J.M.; Sclavounos, P.D. *Development of Fully Coupled Aeroelastic and Hydrodynamic Models for Offshore Wind Turbines*; Technical Report No NREL/CP-500-39066; National Renewable Energy Laboratory: Golden, CO, USA, 2006.
26. Jonkman, J.; Butterfield, S.; Musial, W.; Scott, G. *Definition of a 5-MW Reference Wind Turbine for Offshore System Development*; Technical Report No NREL/TP-500-38060; National Renewable Energy Laboratory: Golden, CO, USA, 2009.
27. Fang, M.-C.; Chen, R.-Y. Three-dimensional solution of the diffraction force on a ship in wave. In Proceedings of the Eighth International Offshore and Polar Engineering Conference: International Society of Offshore and Polar Engineers, Montreal, QC, Canada, 24–29 May 1998.
28. Cummins, W. *The Impulse Response Function and Ship Motions*; David Taylor Model Basin: Washington, DC, USA, 1962.
29. Hasselmann, K.; Barnett, T.; Bouws, E.; Carlson, H.; Cartwright, D.; Enke, K.; Ewing, J.A.; Gienapp, H.; Hasselmann, D.E.; Kruseman, P.; et al. Measurements of wind-wave growth and swell decay during the Joint North Sea Wave Project (JONSWAP). *Ergänzungsheft* **1973**, 8–12.

30. Ramachandran, G.; Robertson, A.; Jonkman, J.; Masciola, M. Investigation of response amplitude operators for floating offshore wind turbines. In Proceedings of the Twenty-third International Offshore and Polar Engineering Conference: International Society of Offshore and Polar Engineers, Alaska, AK, USA, 30 June–5 July 2013.
31. Lee, C.-H. *WAMIT Theory Manual*; Massachusetts Institute of Technology: Cambridge, MA, USA, 1995.
32. Ruzzo, C.; Fiamma, V.; Collu, M.; Failla, G.; Nava, V.; Arena, F. On intermediate-scale open-sea experiments on floating offshore structures: Feasibility and application on a spar support for offshore wind turbines. *Mar. Struct.* **2018**, *61*, 220–237. [[CrossRef](#)]
33. Ruzzo, C.; Fiamma, V.; Nava, V.; Collu, M.; Failla, G.; Arena, F. Progress on the experimental set-up for the testing of a floating offshore wind turbine scaled model in a field site. *Wind Eng.* **2016**, *40*, 455–467. [[CrossRef](#)]
34. Belibassakis, K. A boundary element method for the hydrodynamic analysis of floating bodies in variable bathymetry regions. *Eng. Anal. Bound Elem.* **2008**, *32*, 796–810. [[CrossRef](#)]
35. Shim, S.; Kim, M. Rotor-floater-tether coupled dynamic analysis of offshore floating wind turbines. In Proceedings of the Eighteenth International Offshore and Polar Engineering Conference: International Society of Offshore and Polar Engineers, Vancouver, BC, Canada, 6–11 July 2008.
36. Tracy, C.C.H. *Parametric Design of Floating Wind Turbines*; Massachusetts Institute of Technology: Cambridge, MA, USA, 2007.



© 2019 by the authors. Licensee MDPI, Basel, Switzerland. This article is an open access article distributed under the terms and conditions of the Creative Commons Attribution (CC BY) license (<http://creativecommons.org/licenses/by/4.0/>).